PCCP

Accepted Manuscript

ROYAL SOCIETY OF CHEMISTRY

www.rsc.org/pccp

Aggregation-induced Preparation of Ultrastable Zinc Sulfide Colloidal Nanospheres and Their Photocatalytic Degradations of Multiple Organic Dyes

*Wanting Yang, Xiaoli Liu, Dong Li, Louzhen Fan, and Yunchao Li**

Department of Chemistry, Beijing Normal University, Beijing, 100875 (P. R. China)

Email: liyc@bnu.edu.cn

ABSTRACT: Monodispersed and ultrastable colloidal ZnS nanospheres (NPs) composed of tiny nanoparticles were successfully synthesized by using a limited ligand-induced in-situ aggregation strategy. With such strategy, the whole size as well as the particle size of those ZnS NPs could be tuned simultaneously by properly varying the reaction conditions. Three representative ZnS NP samples with different sphere sizes and particle sizes were thus obtained, which were all proven to possess rather large surface areas, robust structures and excellent colloidal stability. Furthermore, the photocatalytic activities of the as-prepared ZnS NPs toward the photodegradation of eosin B, methylene blue and their binary mixture were explored respectively. An interesting size-dependent degradation performance associated with the ZnS NPs was observed in all the photodegradation cases. Finally, their degradation mechanism was fully elucidated according to the control experiments under different atmospheres in combination with the related energy level information. We believe that the control strategy for tuning the fine and whole structures of spherical nanostructures in a synergetic manner together with the structure-dependent photodegradation performance revealed herein will definitely benefit the fabrication of high-efficient photocatalysts as well as the nanocomplexes of hierarchical architectures.

Key Words: ZnS colloidal nanosphere, in-situ aggregation, organic dye photodegradation, structure-dependent photodegradation performance, photodegradation mechanism

1. Introduction

As one special kind of superparticles, ZnS spherical nanostructures (SNTs), including

microspheres (MPs) and nanospheres (NPs), are well-known for their unique optical properties, large surface areas, uniform morphologies, robust structures and good environment compatibilities. Such features endow ZnS SNTs with special merits in many fields ranging from photonic crystal fabrication,[1, 2] pollutant photocatalytic degradation,[3-8] photocatalytic water splitting,[9, 10] catalytic organic synthesis,[11] to drug delivery and live cell imaging,[12] antibacterial application.[13] It is generally believed that those fascinating performances associated with ZnS SNTs are strongly dependent on their fine structures as well as their huge surface areas. Therefore, in the past decades, great efforts have made to prepare uniform ZnS SNTs of complex secondary structures in order to obtain the largest possible surface areas and as many as possible active sites. Up to now, the established routes for preparing ZnS SNTs include hydrothermal method,[14] aggregated assembly,[15-21] microwave-assisted method,[22] and soft and hard template; [23, 24] high-quality ZnS SNTs with hierarchical architectures,[3, 22, 25-27] porous surfaces,[7, 12, 15, 28-30] hollow interiors[31-35] and additional satellite particles,[4, 7] have been respectively fabricated. However, more and more experimental evidences indicate the fascinating optical and catalytic properties of ZnS SNTs are also seriously limited by their structure robustness, colloidal stability and collectability. In fact, from the practical application point of view, the ideal ZnS SNTs for solution-based application (especially for photocatalysis) should possess the following features simultaneously: large surface area, as many as possible active site, robust structure, good colloidal stability, easy recollection, and good recyclability. Among those features, the surface area and active site are closely related to the secondary (fine) structure of ZnS SNTs, while the other features are mainly dependent on the whole size and the surface state of ZnS SNTs. Therefore, the sophisticated control over the fine and whole structure of ZnS SNTs in a synergetic manner is of particular importance to their overall photocatalytic performances, as it is a rather effective ways to endow the SNTs with all the required optimized features. Unfortunately, not only the importance of such sophisticated control has not yet fully appreciated, but also the protocol to achieve such control is shortage. As a result, the as-prepared ZnS SNTs generally own huge surface areas but large whole sizes as well (from hundreds of nm to several μm), which are more suitable to be referred to as microspheres (MPs).[3, 26, 36-38] Upon application, those ZnS MPs either easily deposit from solution (less than 10 min without stirring) or require continuous stirring to maintain their solubility due to their poor colloidal stability. Apparently, the deposition of ZnS MPs will seriously impair their practical catalytic effect, while their continuous

stirring will cause additional energy consumption. Therefore, it is imperative to develop effective synergetic control strategies to prepare ZnS SNTs of medium-sized whole structures but tiny secondary structures, for the reason that such SNTs may possess the required features and be suitable for long-termed catalytic application.

With the rapid development of textile, paper-making and the related industries, organic dye contaminants have spread widely in the water and soil in many places, posing severe adverse effects on human health and ecosystem due to their non-biodegradability and persistent toxicity.[39, 40] In terms of organic dye removal, photocatalytic degradation technology has shown special advantages (such as low cost, low secondary pollution and good recyclability) over other methods, thus it has drawn considerable interest in the past decades. [3-8, 26-30, 41, 42] However, its wide application still suffers from the shortage of low-cost and high-efficient photocatalyst, although TiO_2 has been identified and employed as a popular catalyst since 1972.[43] It seems that ZnS SNTs of special structural and colloidal features are promising alterative to TiO_2. Unfortunately, as mentioned above, the currently-prepared ZnS SNTs have not yet fully met the practical requirement because of their poor colloidal stability. Moreover, the current studies mainly focus on the investigation of the photodegradation of single dye in each round, which is clearly not competent for treating the real wastewater containing multiple dyes. Besides this limitation, the mechanism of Zn SNTs photocatalytic degradation of dyes has not yet fully clarified though much effort has made to this topic.

In this paper, we develop a limited ligand-induced in-situ aggregation strategy, which allows the secondary and entire structures of target materials to be tuned simultaneously, for preparing the medium-sized ZnS nanospheres (NP_S) consisting of tiny nanoparticles. Three different sizes of ZnS NP_S were thus obtained, which were all confirmed to possess rather large surface areas, robust structures and excellent colloidal stability. Furthermore, the photocatalytic activities of those ZnS NP_S toward the photodegradation of single dye and binary mixed dyes were systemically explored; their attractive size-dependent degradation behaviors were revealed accordingly. Finally, their degradation mechanism was fully elucidated according to the control experiments in combination with the related energy level information. We believe that the control strategy for tuning the fine and whole structures of spherical nanostructures in a synergetic manner together with the structure-dependent photodegradation performance demonstrated herein will definitely benefit the

fabrication of high-efficient photocatalysts as well as other three-dimensional (3-D) nanoassemblies. To the best of our knowledge, this is the first time to report the photodegradation of binary dyes mixture by ZnS NPs, greatly augmenting their potential for real photocatalytic application.

2. Experimental Section

2.1 Materials and Preparation

Materials: Zinc oleate ($Zn(Ol)_2$), oleic acid, methanol, chloroform, toluene, sodium citrate,TiO_2 powder and ZnS powder are analytical grade reagents and were purchased from Beijing Chemical Reagent Ltd. Co. of China. Sulfur powder, tri-*n*-octylamine (TOA, 95%), octadecene (ODE, tech.90%), and trioctylphosphine (TOP, tech.90%) were ordered from Alfar and used as received without any further purification.

Synthesis of the ZnS nanospheres: a specific amount of zinc oleate (0.3 – 0.7 mmol) was dissolved in 6 mL TOA in a 25 mL three-neck round-bottom flask and was degassed at 120 °C for ca. 30 min until the flask was completely vacuumed. Afterwards, the reactant was heated to 295 °C under N_2 atmosphere, and then S precursor (a certain amount of S powder dissolved in 1mL TOP) was rapidly injected into the reaction system at such temperature. After injection, the reaction system generally dropped to ca. 280 °C and was kept at such temperature for 3–5 min. It should be noted that continuous and intensive stirring are necessary in above synthesis process.

Purification of ZnS nanospheres: after reaction, the colloid solutions obtained in above experiments were cooled, and precipitated by methanol. The formed flocculent solutions were centrifuged and their upper liquids were decanted; after that the isolated solids (i.e., ZnS nanospheres) were re-dispersed in chloroform. The above centrifugation and isolation procedure was repeated several times for purification of the as-prepared ZnS nanospheres. Finally, the purified samples were re-dispersed in chloroform for the preparation of TEM and SEM specimens or dried under vacuum for XRD, XPS and FTIR characterization.

Ligand exchange for ZnS nanospheres: the purified ZnS nanospheres were added into a 25 mL flask containing 0.1 M sodium citrate solution. The solutions were maintained at 40 °C and continuously stirred for 1 h to allow ligand exchange to occur on ZnS nanospheres. Afterwards, the ZnS nanospheres overcoated with citrate groups were separated by centrifuging and were finally dissolved in water.

2.2 Characterization and Measurements

UV-vis absorption spectra were recorded on a UV-2450 spectrophotometer, while infrared spectra were recorded on an IRAffinity-1 FTIR with 4 cm^{-1} resolution. The samples for FTIR measurement were prepared by dispersing nanosphere samples or pure ligands in a KBr pellet. Scanning electron microcopy (SEM) characterization was done by using a HITACHI S-4800 scanning electron microscope with an X-ray energy disperse spectroscopy (EDS). Transmission electron microscopy (TEM) observations were performed with a FEI G20 high-resolution transmission electron microscope operated at 200 kV, accompanied by a selected area electron diffraction (SAED). The SEM specimens were prepared by adding drops of dilute solution of ZnS nanospheres on Si substrates. The specimens for TEM observation were prepared by depositing a drop of a dilute toluene solution of these samples on a carbon-coated copper grid and drying at room temperature. X-ray diffraction (XRD) patterns were recorded by a Rigaku D/max-2400 diffractometer operated at 40 kV and 200 mA current with $Cu_{K\alpha}$ radiation (λ=1.5418Å). XPS spectra were obtained on an ESCALAB MK spectrometer equipped with a hemisphere analyzer. The samples for XRD and XPS measurements were all purified solid powders. Cyclic voltammograms were recorded on a Zahner Zennium electrochemical workstation with a conventional three-electrode system according to a previously reported procedure.[18, 44] The total carbon (TC), total organic carbon (TOC) and total inorganic carbon (TIC) content in solutions were measured by a SHIMADZU TOC-V_{CSN} total organic carbon analyzer.

2.3 Photocatalytic Testing.

To evaluate their photocatalytic activities, 10 mg of ZnS nanospheres, commercial ZnS powder and TiO_2 powder were added into 10 mL solutions containing a specified concentration of organic dye (eosin B, methylene blue or their binary mixture) respectively, and such solutions were then irradiated together under a 125 W high-pressure mercury lamp (which was mounted 5.0 cm over the solution and emitted 316~385 nm UV light with a peak around 365 nm). Prior to irradiation, the solutions were continuously stirred for ca. 30 min in the dark to establish an adsorption-desorption equilibrium between the photocatalysts and the dye molecules. It should be noted that all the photodegradation reactions were open to air (or purged with gases) and did not require any stirring. During the photodegradation process, a small aliquot was withdrawn from the solutions at regular

time intervals and was then centrifuged to remove the catalysts. The concentration of the resident dye in such aliquot was further estimated by measuring its absorption spectrum.

3. Results and Discussion

3.1 Morphology and Size Control of ZnS Nanospheres

The recently-developed limited ligand-induced aggregation strategy has demonstrated to be an effective and straight-forward method for the preparation of nanometer- or micrometer-scaled spherical aggregates.[15-21] This in-situ aggregation strategy typically involves two sequential dynamic processes: the first one is the nucleation of initial clusters and their rapid growth into primary nanoparticles in a supersaturated solution by injecting S precursor into a hot solution of Zn precursor; the second one is the aggregation of those primary particles to form ZnS superparticles (i.e., nanospheres) as a result of limit ligand protection. However, until now, it is still a technical challenge to simultaneously control the size of primary particles and of whole structures of ZnS nanospheres at will by using this strategy, as a delicate tune of particle nucleation, growth and aggregation must be reached before achieving such control. To prepare the medium-sized ZnS nanospheres consisting of tiny primary particles, we plan to choose the precursors of appropriate concentration and reactivity in combination with a relative high injection temperature and a weak coordination environment to induce explosive nucleation and rapid particle aggregation.

We and other groups have identified that the thermolysis of long-chained carboxylic zinc and TOPX (X=Se, and Te) in ODE or TOA at relative high temperature enables the formation of spherical ZnX nanostructures.[17, 18, 20] In this paper, we have confirmed that such protocol can be extended to prepare ZnS nanospheres. However, under similar temperature and solvent condition, it was found that Zn and S precursor concentration and their molar ratio also exert a significant influence on the monodispersity and size of ZnS NPs. As shown in Fig. S1 and Table S1, it is clear that the Zn/S molar ratio of 0.5 is favorable to the formation of uniform nanospheres (with a monodispersity of around 10%), while other Zn/S molar ratios generally result in poor size distribution (with a monodispersity of larger than 30%). So, we fixed Zn/S molar ratio at 0.5 in the following synthetic reactions to produce high-quality ZnS nanospheres with required features. Fig. 1 reveals that the average size of ZnS NPS was increased monotonically (from 97 to 177 nm) at first and then decreased after reaching a maximum (177 nm), with increasing the Zn precursor

concentration from 0.031 to 0.052 g/mL in the reaction system. If further increasing $Zn(OL)_2$ concentration, the ZnS nanospheres with multimer structures were obtained. It is worth mentioning that the whole sizes of ZnS NPs prepared in above cases are located in the size range of 90 – 180 nm; the NPs within such size range are typically subjected to slight gravitational influence, thus they may possess the wanted features like good colloidal stability, easy recollection and large surface area. As for the non-monotonical size variation phenomenon, it is probably the result that compromises all the related competitive processes, like nucleation, particle growth and particle aggregation. For the reaction system containing low concentration of Zn and S precursor, only small amount of nuclei were generated upon nucleation; such nuclei then grew slowly and aggregated spontaneously into nanospheres in a few minutes due to the shortage of ligand protection. With increasing the initial precursor concentrations, more nuclei would produce upon nucleation, thus allowing more particles to assembly together and to form big-sized nanospheres. However, if the initial precursor concentrations were too high, many more nuclei would form upon nucleation; so the medium-sized nanospheres were generated as the result of much faster particle aggregation in this case.

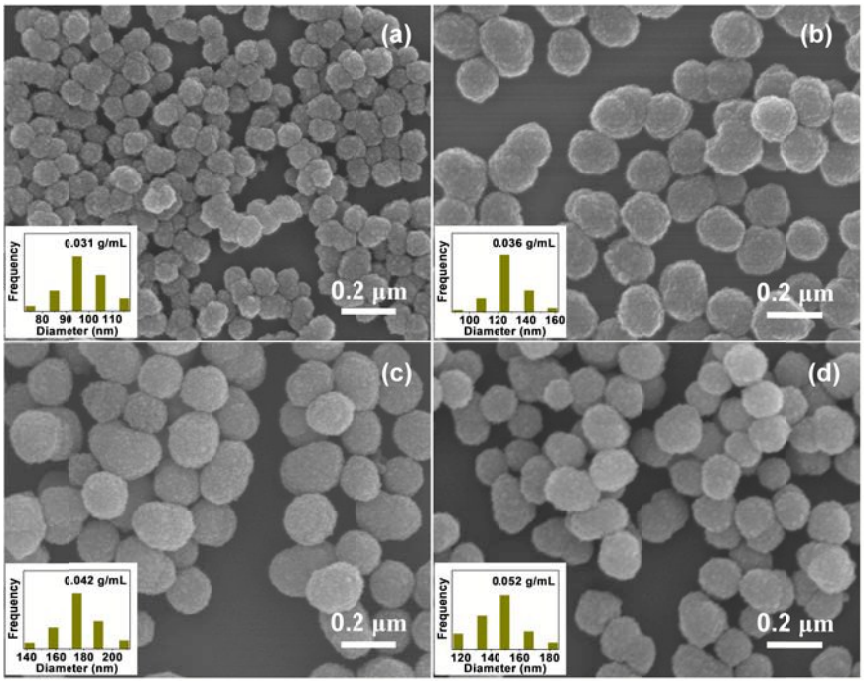

Fig. 1 SEM images of the ZnS nanospheres prepared with using different concentrations of $Zn(Ol)_2$: (a) 0.031 g/mL, (b) 0.036 g/mL, (c) 0.042 g/mL and (d) 0.052 g/mL. In each case, the inset is the corresponding size distribution diagram; the concentration of S precursor is twice of that of Zn precursor.

3.2 Fine Structure and Phase Structure of ZnS Nanospheres

To better understand the fine structure of the as-prepared ZnS nanospheres, we have employed high-resolution SEM and TEM to investigate the ZnS nanospheres with an average size of 147 nm as an example. As shown in Fig. 2, SEM image along with TEM images confirm again the formed products are uniform nanospheres with rough surfaces. EDS result (Fig. S2) reveals the atomic ratio of Zn to S in those nanospheres is 1.3: 1, which is slightly deviated from the stoichiometric ratio in ZnS. Closer inspection (HRTEM) further unveils the nanospheres are actually of polycrystalline nature as expected with many tiny particles (3.0~4.0 nm) randomly and closely packing inside. Careful analysis of the lattice fringes of those particles gives an interplanar spacing of 0.31 nm, which corresponds well to the distance of the (111) lattice plane of standard zinc blend ZnS.[45] The selected area electron diffraction (SAED) pattern, taking from a randomly chosen nanosphere, exhibits characteristic (111), (220) and (311) diffraction rings, reconfirming the polycrystalline architecture of the nanospheres. In fact, the zinc blend polycrystalline structures of the ZnS NPs were also detected by powder XRD analysis (Fig. S4) with giving characteristic and broadened (110), (220), (311) diffraction peaks.[45] It should be noted that the other sized ZnS NPs were also confirmed to possess similar hierarchical architectures composed of tiny particles (Fig. S3).

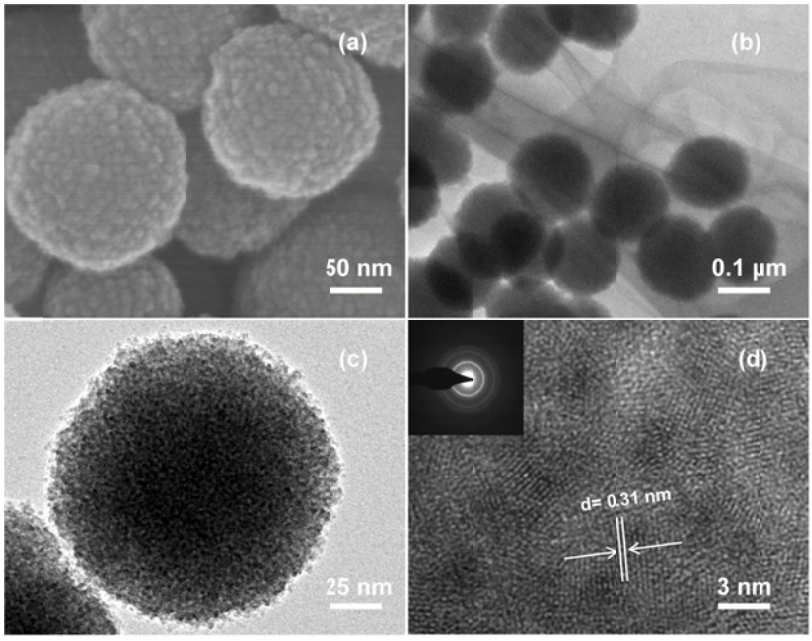

Fig. 2 High resolution characterization of ZnS nanospheres with a diameter of 147 nm**:** (a) high-magnification SEM image, (b) low-magnification TEM image, (c) high-magnification TEM image, and (d) HRTEM image (the inset is the ED pattern of a randomly selected nanosphere).

3.3 Ligand Exchange and Surface Analysis of ZnS Nanospheres

As ZnS NPs were all synthesized in organic solvents, they typically require ligand exchange to improve their solubility in aqueous solutions. Fourier transform infrared spectroscopy (FTIR) results (Fig. 3(a)) reveal that the original ZnS nanospheres (after washing) were co-coated by TOA (evidenced by the presence of strong and characteristic stretching vibration of C-N bond at 1376 cm^{-1})[18] and oleate group (evidenced by the presence of the asymmetric and symmetric stretching vibration of carboxylate group at 1540 cm^{-1} and 1400 cm^{-1}).[18, 46, 47] After ligand exchange, the characteristic vibration of C-N bond disappeared and meanwhile the vibration strength of CH_2 group at 2930 and 2855 cm^{-1} decreased significantly, indicating that short-chained citrate group is the major ligand for the ZnS NPs. XPS spectrum (Fig 3(b)-3(c)) were also employed to examine the surface status of the ZnS NPs before and after the ligand exchange. It is clear that the C spectrum of the original ZnS NPs is composed of three peaks (i.e., strong C=C and C-C peak, and weak C=O peak, while only two strong peaks (i.e., C-C, and C=O peak) can be identified in the C spectrum of the ZnS NP_S after ligand exchange, [48, 49] suggesting the replacement of oleate group by citrate group. In addition, the N spectrum was also found to disappear after the ligand exchange, confirming the removal of the TOA during such process (Fig. S4(c)). A more direct proof for this surface conversion is that the hydrophobic ZnS NPs became water soluble after surface exchange. Clearly, such surface conversion will benefit the subsequent application of ZnS NPs for solution-based photocatalytic degradation.

Furthermore, the surface porosity and area of as-prepared ZnS NPs of different sizes were characterized by N_2 absorption and desorption assays. As shown in Fig. 3(d), there are short of obvious hysteresis loops in all the isotherms, indicating all the ZnS NPs are closely-packing nanospheres without porous structures. According to those isotherms, the BET specific surface areas of the ZnS NPs with a size of 97, 147 and 177 nm and of ZnS commercial powder are estimated to be 10.2, 33.2 ,73.1 and 16.4 $m^2 \cdot g^{-1}$, respectively. It is surprised to find out that the big-sized ZnS nanospheres generally possess a larger specific surface area, which is opposite to the general rule that small particle typically has a larger specific surface area compared to large particle. We think that the special architectures owned by the ZnS nanospheres may account for this interesting phenomenon. As the nanospheres are composed of small nanoparticles, their surface areas are the total surface areas of the particles exposed outside the nanospheres rather

than that of the particles making up them. The big-sized nanospheres allow more particles exposed outside of them, thus they typically have larger specific surface areas.

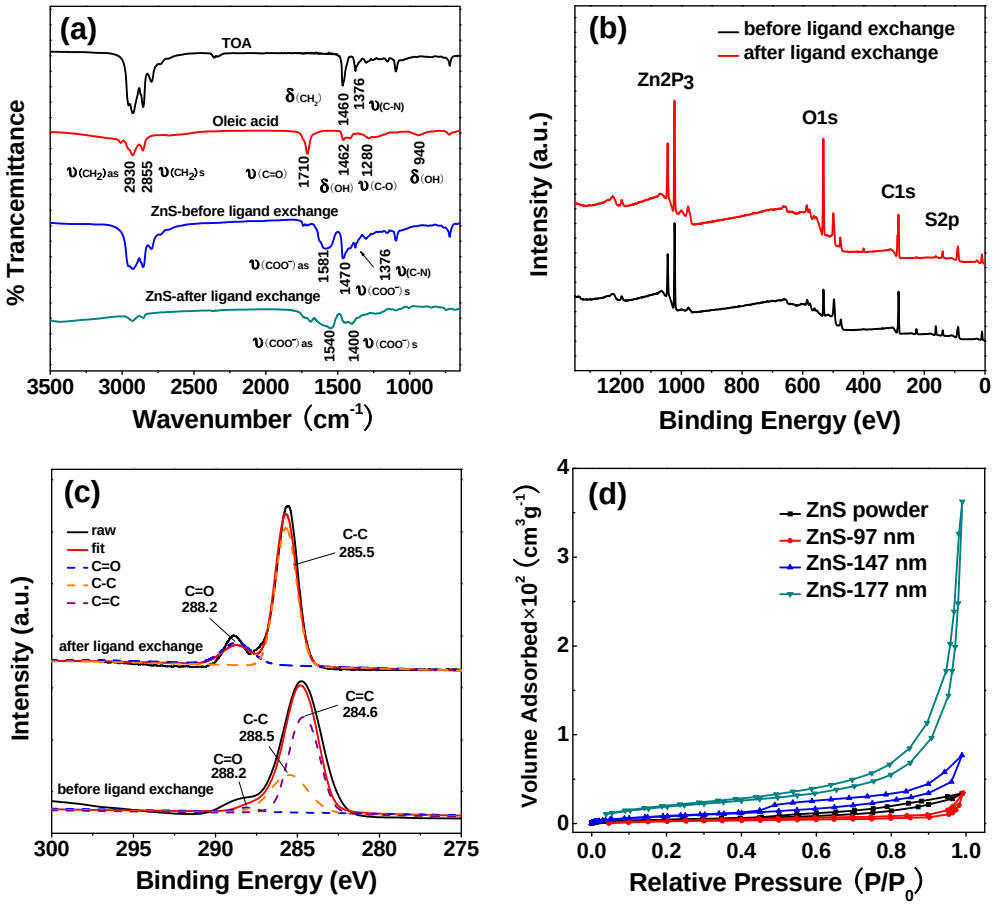

Fig. 3 (a-c) Surface analysis of ZnS nanospheres with a diameter of 177 nm before and after ligand exchange: (a) FTIR spectra, (b) the full range of XPS spectra, and (c) XPS spectra of C1s peak. (d) Nitrogen adsorption-desorption isotherms of ZnS nanospheres of different sizes (after ligand exchange).

3.4 Colloidal Stability and Structure Robustness of ZnS Nanopsheres

As mentioned above, when nanomaterials are employed as solution-based catalyst, their colloidal stability and structure robustness will significantly influence their practical photocatalytic performance. To evaluate their colloidal stability, we dispersed the as-prepared ZnS NPs and commercial ZnS powder in water respectively and tested their maximum suspension times. As shown in Fig.4, it can be observed that all of the commercial ZnS powders precipitated naturally in 20 min; while the ZnS NPs could suspend steadily in water at least for 24 h (still having characteristic Tyndall effect) without any stirring, indicating their excellent colloidal stability. We believe the excellent stability of the ZnS NPs may stem from their medium whole sizes as well as proper surface

states. Zeta potential (ξ) measurements provide a direct proof for this opinion: the zeta potential of the ZnS NPs with a size of 97, 147 and 177 nm were found to be -39, -37 and -35 mV respectively, whose absolute values are obviously large than that of the ZnS powder (13 mV) and most of previous reported values.[13] However, with time prolongation, all of the ZnS NPs could precipitate naturally from the solution (36 h after dispersion), confirming their easy recollection feature (not require any additional assistance). It is the special ability to combine excellent colloidal stability and easy recollection together that sets the as-prepared ZnS NPs apart from previously reported ZnS SNTs.

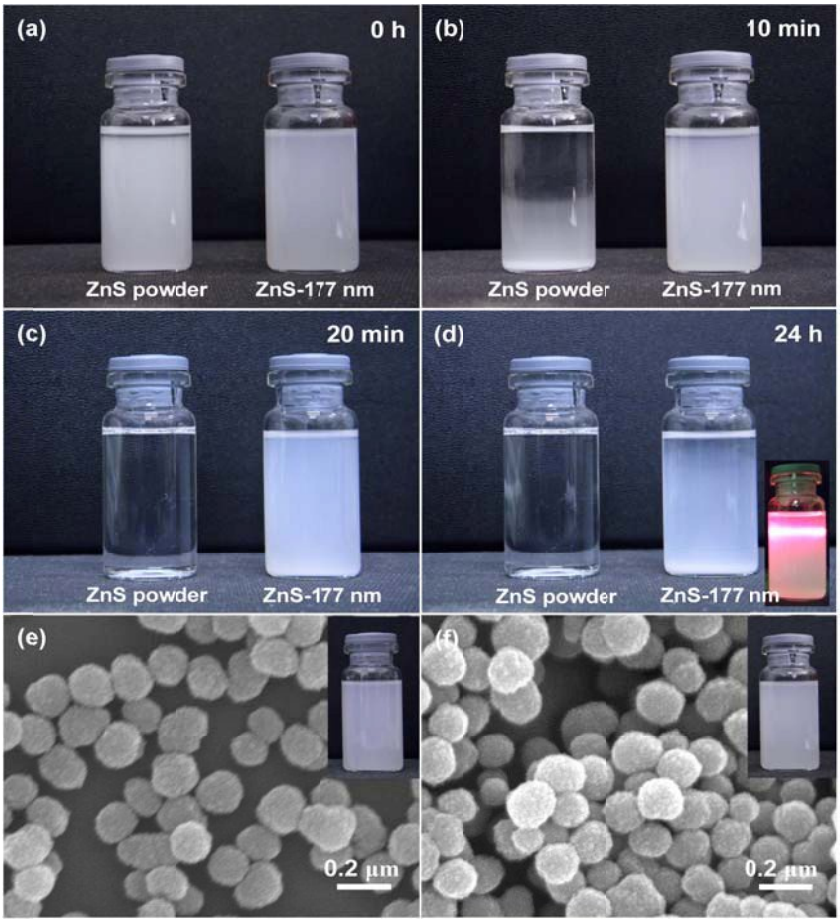

Fig. 4 (a-d) A representative optical image to show the suspension stability of ZnS nanospheres with a diameter of 177 nm and commercial ZnS powder dispersed in water for different times, (a) 0 min, (b) 10 min, (c) 20 min and (d) 24 h (the inset is aimed to show the Tyndall effect of such solution). (e-f) A representative SEM image to show the morphology of the ZnS NPs under different UV irradiation times, (e) 0 min and (f) 24 h.

When it comes to the practical application of a photocatalyst, its structure robustness must be taken into account. As shown in Fig. 4, after exposure to UV irradiation (120 W) for 24h, the as-prepared ZnS NPs did not show any discernible variation in their morphologies and colloidal

dispersion properties (even their surface-coated citrate groups were found to be almost intact, see Fig. S5), demonstrating their excellent structure robustness and colloidal stability.

3.5 Optical and Electrochemical Properties of ZnS Nanospheres.

It is well-known that the size and bandgap information of semiconductor nanomaterials can be easily acquired by measuring their absorption spectra. The UV-vis absorption spectra of the as-prepared ZnS NPs are shown in Fig. 5(a), from which it can be observed all curves exhibit a distinct shoulder peak around 300 nm followed by a long tail at the longer wavelength side. Clearly, the shoulder peak is attributed to the band edge absorption from the ZnS nanoparticles composing the spheres, while the long absorption tail is due to the Mie scattering from the spheres themselves. It is interesting to find that the shoulder peak is generally red-shifted with increasing the size of the nanosphere, indicating the big-sized nanospheres probably consisting of big-sized nanoparticles. To get clearer bandgap information on the ZnS NPs, we converted their UV-vis spectra to the corresponding Tauc plots.[50] As shown in Fig. 5(b), the band gap can be estimated by extrapolating the linear portions of the curves to the energy axis according to the equation of

$$Ah\nu = B(h\nu - E_g)^{1/2} \qquad (1)$$

where α is the absorption coefficient, hν is the photon energy, E_g is the direct band gap energy, and B is a constant. With this method, the optical band gaps of ZnS nanospheres with a diameter of 97, 147 and 177 nm were estimated to be 4.0, 3.9 and 3.8 eV, respectively.

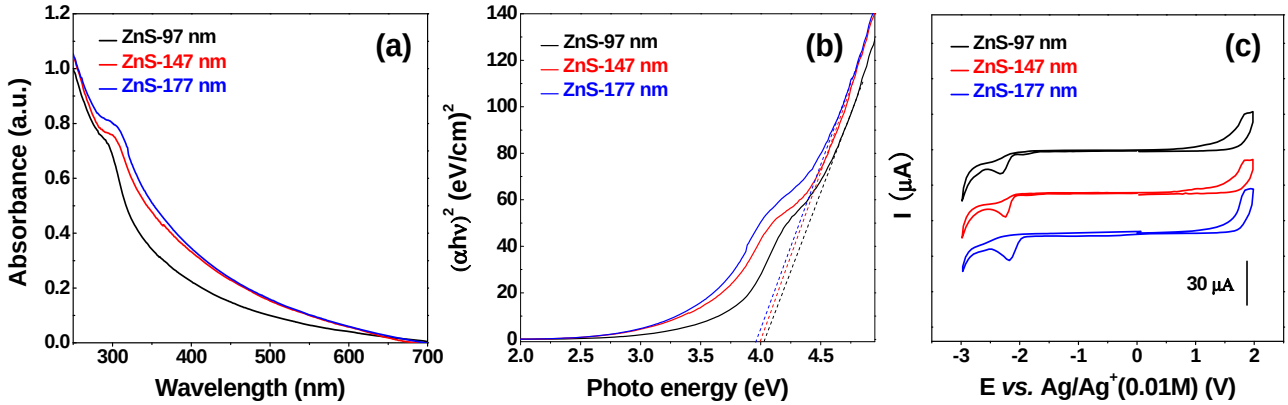

Fig. 5 (a) Absorption spectra, (b) Tauc plots, and (c) cyclic voltammograms of ZnS nanospheres with different sizes.

Electrochemical cyclic voltammetry (CV) is a direct and powerful tool to estimate the absolute energy values of valence band edge (E_{vb}), conduction band edge (E_{cb}), and bandgap (E_{gap}) of

electroactive species including semiconductor nanomaterials.[18, 44,51, 52] The E_{vb} and E_{cb} energy levels of ZnS nanospheres can be respectively estimated from the peak potentials of the oxidation and reduction waves shown in their cyclic voltammograms.[51, 52] As shown in Figure 5(c), the three CV curves all demonstrate a pair of well-separated redox peaks. Relative to Ag/Ag^+ reference electrode, the onset oxidation and reduction potentials of those products are 1.88 and -2.34 V for ZnS-97nm NP, 1.85 and -2.26 V for ZnS-147nm NP, 1.82 and -2.18 V for ZnS-177nm NP, respectively. It can be seen that the peak potentials of the anodic and cathodic peaks are generally negatively and positively shifted respectively, with the increase of sphere size. The estimated electrochemical band gaps of the ZnS NPs with a diameter of 97 nm, 147 nm and 177 nm are 4.22 eV, 4.1 eV and 4.0 eV, respectively.

As long as knowing their bandgap information, we could calculate the size of the nanoparticles composing the nanospheres according to Brus equation,

$$E_{n,gap} = E_{b,gap} + (\hbar^2\pi^2/2R^2)(1/m_e^* + 1/m_h^*) - 1.786e^2/4\pi\varepsilon_0\varepsilon R \qquad (2)$$

where $E_{n,gap}$, $E_{b,gap}$, R, m_e^* and m_h^* are the bandgap energy for a ZnS nanoparticle and its bulk counterpart, the radius of the particle, and the effective mass of electron and hole in the particle, respectively.[53] Based on the bandgap values obtained from the aforementioned optical and electrochemical characterizations, the average size of the particles inside in the three different-sized nanospheres were calculated and listed in Table 1. For the purpose of comparison, those nanosphere samples were also examined by HRTEM (see Fig. S3) and the obtained particle sizes were included in Table 1 as well. It can be observed that the particle sizes determined by the three methods are well consistent with each other besides they all exhibit a similar increasing trend with the increase of sphere size (i.e., $d_{ZnS\text{-}97nm} < d_{ZnS\text{-}147nm} < d_{ZnS\text{-}177nm}$).

Table 1 E_{vb}, E_{cb} and E_{gap} values of the ZnS nanospheres and their corresponding particle sizes

Sample	Optical bandgap		Electrochemical bandgap			Particle diameter		
	Abs /nm	E_{gap}^{opt}/eV	E_{cb}/eV	E_{vb}/eV	E_{gap}^{el} /eV	d_{opt}/nm	d_{el}/nm	d_{TEM}/nm
ZnS-97nm	310	4.0	-6.59	-2.37	4.22	3.4	3.5	3.2
ZnS-147nm	318	3.9	-6.56	-2.45	4.11	3.7	3.9	3.4
ZnS-177nm	326	3.8	-6.53	-2.53	4	4.1	4.4	3.7

3.6 Photocatalytic degradation performance

Photocatalytic degradation has proven to be an effective, low-cost and environment-benign means to eliminate toxic organic chemicals from environment. To evaluate the photocatalytic performance of the as-prepared ZnS NPs, eosin B (EB) was selected as a target organic contaminant and its characteristic absorption (λ=517 nm) was chosen to monitor the whole degradation process. For the purpose of comparison, a series of control experiments, such as the degradation in the absence of any light or catalyst, the degradation with using commercial catalysts (ZnS and TiO_2 powder), were also performed under the same conditions. As shown in Fig. S6 and Fig.6, it is clear that the degradation of EB was negligible in the dark and was low efficient (ca. 70% degradation after 9.0 h of illumination) under UV-light irradiation in the absence of catalyst (self-degradation). As the commercial ZnS and TiO_2 powder were employed as the catalyst, it typically took ca. 8.0 and 9.0 h to completely degrade EB, respectively. In contrast, with the induction of the as-prepared ZnS NPs into such process, the photodegradation of EB was found to be significantly accelerated. It only needed 2.0, 4.5, and 5.5 h to completely degrade EB (losing all the characteristic absorptions and becoming colorless) under the same UV irradiation condition with the presence of 177, 144, 97 nm ZnS NPs, respectively. The complete degradation of EB over 177 nm ZnS NPs was also witnessed by the total organic carbon (TOC) measurement, which shows only ca. 3% TOC remaining in the solution after such photodegradation (see Table S2). To better depict the photocatalytic activity of those materials, the apparent reaction rate was adopted because their photocatalytic degradation reactions typically follow a pseudo-first-order expression:

$$\ln(C_0/C) = kt \qquad (3)$$

where C_0/C is the normalized organic compound concentration and k is the apparent reaction rate (h^{-1}).[8,54] The constant (k) can be obtained by plotting $\ln(C_0/C)$ versus irradiation time and performing linear fitting. According to Fig 6(d), the reaction constants (k) in above cases are 0.14 h^{-1} for self-degradation, 0.36 h^{-1} for using commercial ZnS powder, 0.33 h^{-1} for using TiO_2 powder, 0.75 h^{-1} for using ZnS-97nm NP, 0.86 h^{-1} for using ZnS-147nm NP, and 1.22 h^{-1} for using ZnS-177nm NP, respectively (Table S2). Clearly, the big-sized ZnS NPs generally displayed a higher photocatalytic activity among those materials. Particularly, the ZnS-177nm

NP demonstrated the best photocatalytic performance, whose reaction constant *k* was ca. 3.5 times higher than that of commercial ZnS and TiO_2 powder. This size-dependent photocatalytic performance of those ZnS NP samples can be easily understood by taking their specific surface areas into account. As mentioned above, the BET specific surface areas of those ZnS NPs follow the order of ZnS-177nm NP > ZnS-147nm NP > ZnS-97nm NP. The prominent photo-degradation performance of the ZnS-177nm NP sample is mainly attributed to its considerably large surface area, which allows many more EB molecules to be absorbed and to interact with the generated electrons and holes. In addition, we also noticed that the optical bandgap of this NP sample (ca. 3.8 eV) is the best matched with the wavelength of the adopted UV light (316 ~ 385 nm with an emission peak around 365 nm, see Fig. 8 (a)) among the three NP samples. Therefore, the ZnS-177nm NP sample may have the possibility to produce more electrons and holes on its surface upon undergoing UV illumination, resulting in more efficient degradation of EB.

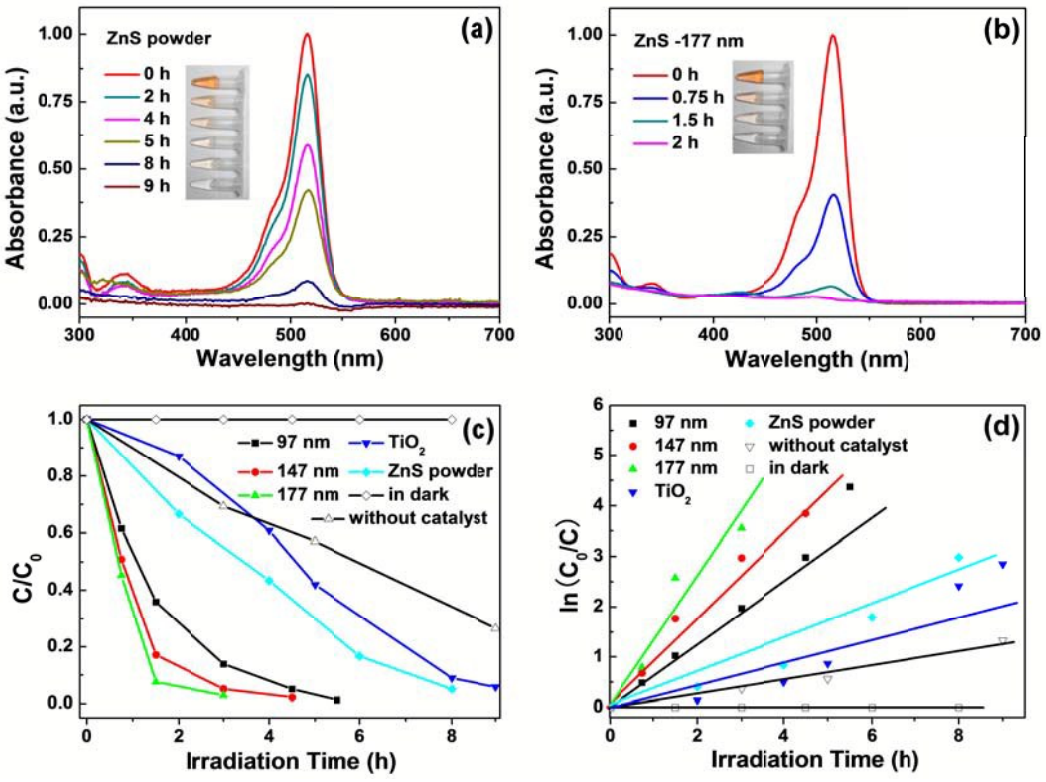

Fig. 6 Temporal UV-visible absorption spectra observed for the solutions (10 mL) containing eosin B (5×10^{-5} M) in the presence of 10 mg of commercial ZnS powder (a) or 177 nm ZnS nanospheres (b). The normalized concentration of eosin B as a function of UV illumination time under different conditions (c), Plots of $\ln(C_0/C)$

of eosin B versus irradiation time, showing the fitting results with using the pseudo-first-order reaction model (d).

In consideration of practical application requirement, we particularly evaluated the recyclability of the as-prepared ZnS NPs by repeatly using them as a photocatalyst. As shown in Fig S6(h), no appreciable decay of the photocatalytic activity was found for those NP samples after they were recycled in the photodegradation of EB for three consecutive runs. In addition, we also confirmed that not only their structures were kept intact but also their colloidal stability were remained after such repeat testing, consistent with the previous observations revealed in Fig. 4(f). Both results indicate the ZnS NPs are competent for the long-termed photocatalytic application.

When methylene blue (MB) was chosen instead of eosin B as the target contaminant, it was found that a slightly longer time (at least 7 hours) was required for the ZnS NPs to completely degrade such dye (evidenced by the solutions losing all the characteristic absorptions, becoming colorless and losing ca. 97.3 % TOC, see Fig. S7 and Table S2) under the same illumination condition. Even so, the ZnS-177nm NP sample still demonstrated the best photodegradation performance among those materials, whose reaction constant *k* (see Table S3) is ca. 4~5 times higher than that of commercial ZnS and TiO_2 powder. As for the reason why a longer time is required for degrading MB, we think this may be ascribed to the more robust molecular structure of MB compared to that of EB.

To fully evaluate the photodegradation performance of the as-prepared ZnS NPs, we have systemically compared their degradation rate, degradation efficiency and degradation condition with those of previously reported analogues (see Table S3). It is clearly that the photo-degradation performance of ZnS-177nm NP sample is slightly inferior to but yet comparable to that of the best catalysts fabricated previously. Moreover, it is also noteworthy that the ZnS NPs prepared herein did not require any stirring during those photodegradation processes because of their excellent colloidal stability, setting them apart from the previously reported catalysts.

The success on the photodegradation of EB and MB individually allows us to explore whether the two dyes could be degraded together by using the as-prepared ZnS NPs. In fact, the

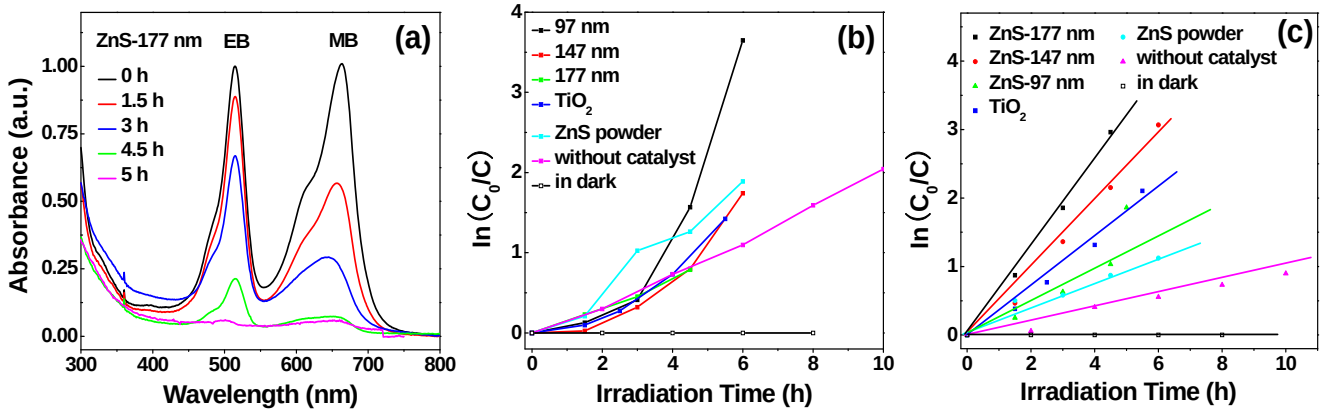

Fig. 7 (a) Temporal UV-visible absorption spectra observed for the methylene blue /eosin B binary system in the presence of 177 nm ZnS nanospheres as a function of illumination time (MB: 5×10^{-5} M; EB: 1×10^{-5} M). Plots of $\ln(C_0/C)$ of eosin B (b) and methylene blue (c) versus irradiation time, showing the fitting results with using the pseudo-first-order reaction model.

simultaneous degradation of two different dyes is highly needed because the real industrial wastewater typically contains multiple dyes. To achieve such goal, we added the ZnS NPs to a solution containing a specific concentration of MB and EB ([MB] / [EB]=5:1) and tracked the evolution of their characteristic absorption peaks (λ_1=517 nm for EO and λ_2=665 nm for MB) with illumination time to monitor their photodegradation processes. As shown in Fig. 7 and Fig. S8, it can be observed that the two characteristic peaks are gradually decreased to zero with the prolongation of illumination time, signifying the complete degradation of the two dyes. Similarly, the ZnS-177nm NP sample still demonstrated the best photodegradation performance among those catalysts. However, it was surprised to find that the degradation of MB was obviously accelerated while that of EB was distinctly postponed in this binary mixed system compared with the corresponding degradation in single dye system (see Table S4). This interesting phenomenon can be explained from the energy level alignment viewpoint (Fig. S9-S10): the E_{cb} (or LUMO) energy level of ZnS NP, EB and MB follow the order of ZnS (-2.45 eV) > EB (-2.72 eV) > MB (-3.51 eV), which are all higher than the redox potential of $O_2/O_2^{\bullet-}$(-3.89 eV).[55] With the coexistence of EB and MB in the solution, upon UV illumination, the excited electrons in ZnS E_{cb} level were more easily transferred to the O_2 molecules in close proximity to the nanospheres by going through the LUMO level of EB and MB sequently. So, MB molecules gained more chances to directly interact with the in-situ produced $O_2^{\bullet-}$ radicals, thus their

degradation processes were accelerated and became dominated at the early stage. On the contrary, the degradations of EB molecules were postponed due to the blocking from MB molecules. A similar phenomenon was observed previously in the simultaneous photo-degradation of eosin Y and rhodamine B over TiO_2 P-25, in which eosin Y played a role similar to that of EB in this case.[5]

3.7 Photocatalytic mechanism

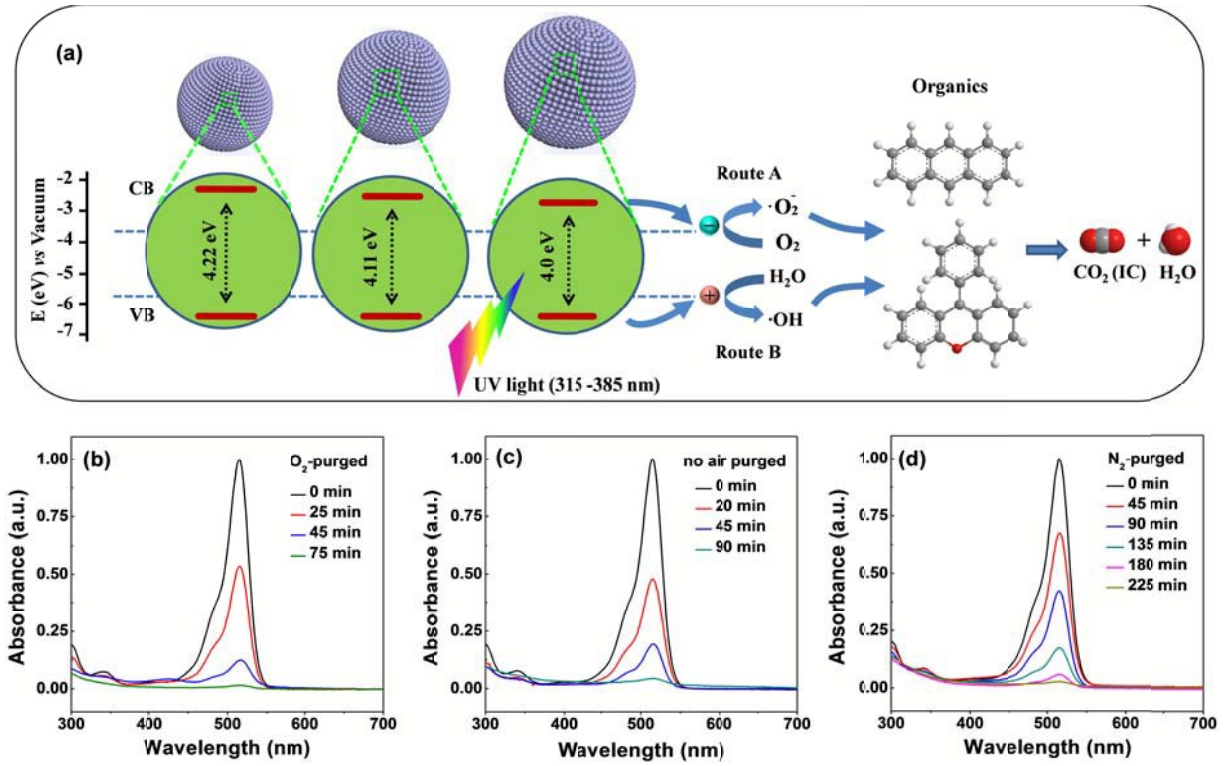

Fig. 8 (a) Schematic illustration of the possible reaction mechanism of the photodegradation of organic dye over ZnS nanospheres. (b-d) Temporal UV-visible absorption spectra to show the photodegradation of eosin B over 177 nm ZnS nanospheres under different atmospheres, (b) O_2-purged condition, (c) open to air (no gas purging), and (d) N_2-purged condition.

It is generally accepted that the semiconductor catalyst-assisted photodegration of organic pollutant probably involves the following steps (see Fig.8 (a))[56, 57]: upon UV illumination, the semiconductor catalyst can absorb photons with energy larger than its bandgap and excite electrons from its valence band to conduction band, thus producing the reductive conduction band electrons (e^-) and oxidative valence band holes (h^+). The formed valence band holes can further react with the surface absorbed H_2O to produce ·OH radical or directly oxide the organics

(Route A); while the conduction band electrons are usually scavenged by the dissolved O_2 to yield superoxide radical ($O_2^{\bullet-}$) (Route B). So, the organic pollutants can be finally broken down into small molecular fragments under the attacking of the formed highly reactive radicals (such as ·OH and/ or $O_2^{\bullet-}$). We think the photodegradation of EB/MB over ZnS NPs demonstrated herein can be also explained by above mechanism. However, it is still not clear whether or not the valence band oxidation reaction (Route A) and the conduction band reduction reaction (Route B) were both involved in such photodegradation processes. Moreover, it also needs to identify which reaction dominated the overall photodegradation process if they both participated in. To solve such questions, we carried out a series of control experiments with using 177 nm ZnS NPs as the catalyst but under different atmosphere in order to facilitate or block the Route A/B intentionally. As shown in Fig. 8(b)-8(d), it can be observed that the degradation rate of EB obviously slowed down after the solution was continuously purged with N_2 to eliminate the dissolved O_2 (i.e., blocking Route B), revealing the existence of valence band oxidation reaction (Route A) in such degradation process. In contrast, the degradation rate was found to be only slightly increased as the solution was continuously purged by O_2 to enhance its concentration therein (i.e., accelerating route B), suggesting the air-equilibrated dissolved O_2 was sufficient for the dye degradation.[5] Those results strongly indicate the valence band oxidation reaction and the conduction band reduction reaction were both actively involved in the photodegradation of EB/MB over ZnS NPs; however, the reduction of dissolved O_2 by conduction band electrons seemed to play a crucial role in such processes.

4. Conclusions

In this paper, we have developed a limited ligand-induced in-situ aggregation strategy for preparing high-quality ZnS nanospheres (NPs) consisting of tiny nanoparticles. By using such strategy, we were able to prepare the ZnS NPs with their whole sizes and affiliated particle sizes ranging from 90 to 180 nm, 3.0 to 5.0 nm respectively, owing to such strategy allowing the secondary and entire structures of the NPs to be tuned simultaneously. Three representative ZnS NP samples with different sizes (97, 147, 197 nm) were thus obtained, which were all confirmed to possess rather large surface areas, robust structures and excellent colloidal stability. Furthermore, the photocatalytic activities of those ZnS NPs toward the photodegradation of

eosin B, methylene blue and their binary mixture were explored respectively. It was interesting to find that the big-sized ZnS NPs generally demonstrated a higher photocatalytic activity in all the degradation cases, which is mainly attributed to their larger specific surface areas as well as to their stronger absorption to the UV light. Besides of excellent photodegradation performance, those ZnS NPs also exhibited a special advantage of not requiring any stirring during photodegradation process, setting them apart from the previously reported catalysts. Finally, according to the control experiments under different atmospheres along with the related energy level information, we revealed that the reduction of dissolved O_2 by conduction band electrons played a crucial role in the photodegradation of such dyes though the valence band oxidation reaction was also actively involved in such process. We believe that the control strategy for tuning the fine and whole structures of spherical nanostructures in a synergetic manner together with the structure-dependent photodegradation performance demonstrated herein will definitely benefit the fabrication of high-efficient photocatalyst as well as other complex nanoassemblies.

Acknowledgements

This work is financially supported by the Natural Science Foundation of China (NSFC, 21273020, 21003012, 91023039, and 21233003 (the State Key Program)).

References

1 J. E. G. J. Wijnhoven and W. L. Vos, *Science*, 1998, **281**, 802-804.

2 K. P. Velikov, A. Moroz and A. V. Blaaderren, *Appl. Phys. Lett.*,2002, **80**, 49-51.

3 Q. Zhao, Y. Xie, Z. Zhan and X. Bai, *Cryst. Growth Des.*, 2007, **7**, 153-158.

4 W. T. Chen and Y. J. Hsu, *Langmuir*, 2009, **26**, 5918-5925.

5 M. Yin, Z. Li, J. Kou and Z. Zou, *Environ. Sci. Technol.*, 2009, **43**, 8361-8366.

6 D. Chen, F. Huang, G. Ren, D. Li, M. Zheng, Y. Wang and Z. Lin, *Nanoscale*, 2010, **2**, 2062-2064.

7 S. Singla and B. Pal, *Mater. Res. Bull.*, 2013, **48**, 4867-4871.

8 Y. P. Zhu, J. Li, T. Y. Ma, Y. Liu, G. Du and Z. Yuan, *J. Mater. Chem. A.*, 2014, **2**, 1093-1101.

9 A. Kudo, *Catal.Surv. Asia*, 2003, **7**, 31-38.

10 R. M. Navarro Yerga, M. C. ÁlvarezGalván, F. Del Valle, J. A. Villoria de la Mano and J. L.

Fierro, *ChemSusChem*, 2009, **2**, 471-485.

11 L. Lang, B. Li, W. Liu, L. Jiang, Z. Xu and G. Yin, *Chem. Commun.*, 2010, **46**, 448-450.

12 R. Xing and S. Liu, *Nanoscale*, 2012, **4**, 3135-3140.

13 G. Li, J. Zhai, D. Li, X. Fang, H. Jiang, Q. Dong and E. Wang, *J. Mater. Chem.*, 2010, **20**, 9215-9219.

14 C. Jiang, W. Zhang, G. Zou, W. Yu and Y. Qian, *Mater. Chem. Phys.*, 2007, **103**, 24-27.

15 W. Jia, X. Wu, B. Jia, F. Qu and H. J. Fan, *Sci. Adv. Mater.*,2013, **5**, 1329-1336.

16 Q. Z. Wu, H. Q. Cao, S. Zhang, X. C. Zhang and X. R. Zhang, *Inorg.Chem.*,2006, **45**, 4586-4588.

17 H. Zhong, Z. Wei, M. Ye, Y. Yan, Y. Zhou, Y. Ding, C. Yang and Y. Li, *Langmuir*, 2007, **23**, 9008-9013.

18 F. Jiang, Y. Li, M. Ye, L. Fan, Y. Ding and Y. Li, *Chem. Mater.*, 2010, **22**, 4632-4641.

19 M. Muruganandham, R. Amutha, E. Repo, M. Sillanpää, Y. Kusumoto and M. Abdulla-Al-Mamun, *J. Photoch. Photobio. A*, 2010, **216**, 133-141.

20 G. Yang, H. Zhong, R. Liu, Y. Li and B. Zou, *Langmuir*, 2013, **29**, 1970-1976.

21 A. Narayanaswamy, H. F. Xu, N. Pradhan and X. G. Peng, *Angew. Chem. Int. Ed.*, 2006, **45**, 5361-5364.

22 Q. Z. Yao, G. Jin and G. T. Zhou, *Mater. Chem. Phys.*, 2008, **109**,164-168.

23 X. W. D. Lou, L. A. Archer and Z. Yang, *Adv. Mater.*, 2008, **20**, 3987-4019.

24 J. Liu, F. Liu, K. Gao, J. Wu and D. Xue, *J. Mater. Chem.*, 2009, **19**, 6073-6084.

25 S. Xiong, B. Xi, C. Wang, D. Xu, X. Feng, Z. Zhu and Y. Qian, *Adv. Funct. Mater.*, 2007,**17**, 2728-2738.

26 M. Sookhakian, Y. M. Amin and W. J. Basirun, *Appl. Surf. Sci.*, 2013, **283**, 668-677.

27 Q. Zhao, Y. Xie, Z. Zhan and X. Bai, *Cryst. Growth Des.*, 2007, **7**, 153-158.

28 M. Muruganandham, A. Ramakrishnan, Y. Kusumoto and M. Sillanpää, *Phys. Chem. Chem. Phys.*, 2010, **12**, 14677-14681.

29 J. S. Hu, L. L. Ren, Y. G. Guo, H. P. Liang, A. M. Cao, L. J. Wan and C. L. Bai, *Angew. Chem. Int. Ed.*, 2005, **117**, 1295-1299.

30 Y. Tian, G. F. Huang, L. J. Tang, M. G. Xia, W. Q. Huang and Z. L. Ma, *Mater. Lett.*, 2012, **83**,104-107.

31 J. Geng, B. Liu, L. Xu, F. N. Hu and J. J. Zhu, *Langmuir*, 2007, **23**, 10286-10293.

32 L. Dong, Y. Chu, Y. Zhang, Y. Liu and F. Yang, *J. Colloid Interface Sci.*, 2007, **308**, 258-264.

33 S. K. Panda and S. Chaudhuri, *J. Colloid Interface Sci.*, 2007, **313**, 338-344.

34 H. Shao, X. Qian and Z. K. Zhu, *J. Solid State Chem.*, 2005, **178**, 3522-3528.

35 H. Zhou, T. Fan, D. Zhang, Q. Guo and H. Ogawa, *Chem. Mater.*, 2007, **19**, 2144-2146.

36 Q. Wu, H. Cao, S. Zhang, X. Zhang and D. Rabinovich, *Inorg. Chem.*, 2006, **45**, 7316-7322.

37 Y. Shi, J. Chen and P. Shen, *J. Alloy Compd.*, 2007, **441**, 337-343.

38 G. Zhang, C. Li, X. Zhang, X. Guo, Y. Liu, W. He, J. Liu, H. Wang and Y. Gao, *RSC Adv.*, 2014, **4**, 13569-13574.

39 B. Neppolian, H. C. Choi, S. Sakthivel, B. Arabindoo and V. Murugesan, *J. Hazard. Mater.*, 2002, **89**, 303-317.

40 S. Chakrabarti and B. K. Dutta, *J. Hazard. Mater.*, 2004, **112**, 269-278.

41 A. Bumajdad and M. Madkour, *Phys. Chem. Chem. Phys.*, 2014, 16, 7146-7158.

42 R. Zamiri, H. Abbastabar, D.M. Tobalsi, A. Rebelo, M. P. Seabra, M. Shabani and J. M. F. Ferreira, *Phys. Chem. Chem. Phys.*, 2014,16,22418-22425.

43 A. Fujishima and K. Honda, *Nature*, 1972, **238**, 37-38.

44 J. Liu, W. Yang, Y. Li, L. Fan and Y. Li, *Phys. Chem. Chem. Phys.*, 2014, **16**, 4778-4788.

45 Y. Li, X. Li, C. Yang, Y. Li X., *J. Phys. Chem. B* 2004, **108**, 16002-16011.

46 N. Q. Wu, L. Fu, M. Su, M. Aslam, K. C. Wong and V. P. Dravid, *Nano Lett*. 2004, **4**, 383-386.

47 S. H. Lee, Y. J. Kim and J. Park, *Chem. Mater*. 2007, **19**, 4670-4675.

48 C. Perruchot, M. M. Chehimi, M. Delamar, S. F. Lascelles and S. P. Armes, *Langmuir*, 1996, **12**, 3245-3251.

49 J. Lu, J. X. Yang, J. Wang, A. Lim, S. Wang and K. P. Loh, *ACS nano*, 2009, **3**, 2367-2375.

50 Y. Wang, A. Suna, W. Mahler, R. Kasowaki, *J. Chem. Phys.* 1987, **87**, 7315-7322.

51 C. Querner, P. Reiss, S. Sadki, M. Zagorska, A. Pron, *Phys. Chem. Chem. Phys.*, 2005, **7**, 3204-3209.

52 S. N. Inamdar, P. P. Ingole, S. K. Haram, *ChemPhysChem,* 2008, **9**, 2574-2579

53 L. E. Brus, J. Chem. Phys., 1984, **80**, 4403-4409.

54 T. Zhang, T. Oyama, A. Aoshima, H. Hidaka, J. Zhao, N. Serpone, *J. Photoch. Photobio. A.,* 2001, **140**, 163-172.

55 A. Fujishima, T. N. Rao and D. A. Tryk, *J. Photoch. Photobio. C.*, 2000, **1**, 1-21.

56 C. Chen, W. Ma, and J. Zhao, Chem. *Soc. Rev.*, 2010, **39**, 4206-4219.

57 P. Qu, J. Zhao, T. Shen and H. Hidaka, *J. Mol. Catal. A: Chem.*, 1998, **129**, 257-268.